



# Slip-cast and hot-solution infiltrated porous yttria stabilized zirconia (YSZ) supported tubular fuel cells



Amir Reza Hanifi<sup>a,\*</sup>, Scott Paulson<sup>b</sup>, Alireza Torabi<sup>a</sup>, Alyssa Shinbine<sup>a</sup>, Michael C. Tucker<sup>c</sup>, Viola Birss<sup>b</sup>, Thomas H. Etsell<sup>a</sup>, Partha Sarkar<sup>d</sup>

<sup>a</sup> Department of Chemical & Materials Engineering, University of Alberta, Edmonton, AB T6G 2V4, Canada

<sup>b</sup> Department of Chemistry, University of Calgary, Calgary, AB T2N 1N4, Canada

<sup>c</sup> Environmental Energy Technologies Division, Lawrence Berkeley National Laboratory, Berkeley, CA 94720, USA

<sup>d</sup> Carbon & Energy Management, Alberta Innovates – Technology Futures, Edmonton, AB T6N 1E4, Canada

## HIGHLIGHTS

- Hot solution infiltration was investigated to form novel anode and cathode components.
- Infiltration of the Ni, Ce and Sm salts into the porous support did not result in complete penetration.
- LSM infiltration appears to be very effective.
- Reasonable power densities considering the infiltrates amounts are achieved.

## ARTICLE INFO

### Article history:

Received 24 February 2014

Received in revised form

19 April 2014

Accepted 1 May 2014

Available online 14 May 2014

### Keywords:

Hot solution infiltration

NiO–SDC

LSM

GDC–LSCF

Porous YSZ

Tubular SOFC

## ABSTRACT

Hot solution infiltration was investigated as a flexible and rapid method to incorporate anode and cathode components into fully sintered, porous ceramic tubular templates for use as solid oxide fuel cells (SOFC). Composed of either a porous 8 mol% yttria-stabilized zirconia (YSZ) or 5 wt% NiO–YSZ support structure, a thin Ni–YSZ anode functional layer and an outer ca. 10  $\mu\text{m}$  dense YSZ electrolyte, closed end tubes were first hot solution (ca. 100 °C) infiltrated on the inside with NiO–SDC ( $\text{Sm}_{0.2}\text{Ce}_{0.8}\text{O}_{1.9}$ ) to serve as the anode. Cathodes were either LSM (nominally  $\text{La}_{0.8}\text{Sr}_{0.2}\text{MnO}_{3+\delta}$ ) infiltrated into a thin porous YSZ layer on the outer electrolyte surface, or an LSCF–GDC composite ( $\text{Gd}_{0.1}\text{Ce}_{0.9}\text{O}_{1.95}$ – $\text{La}_{0.6}\text{Sr}_{0.4}\text{Co}_{0.2}\text{Fe}_{0.8}\text{O}_{3-\delta}$ ) on a thin GDC buffer layer. Although hot solution infiltration of the Ni, Ce and Sm salts into the anode support structure did not result in complete penetration (with the Ni contents in the tube wall ranging between 4 and 10 vol.%), well-sealed full cells produced power densities as high as 275, 196 and 153  $\text{mW cm}^{-2}$  at 800, 750 and 700 °C, respectively. Hot solution infiltration of active SOFC electrode materials is thus shown to be a very flexible approach for the evaluation of their performance.

© 2014 Elsevier B.V. All rights reserved.

## 1. Introduction

Many technologies related to energy storage [1] and fuel cells [2] rely on the combination of electronically conductive and catalytically active materials, usually in porous structures. Solution infiltration into a porous support network offers a low technology method of incorporating electrode materials and structures that otherwise would not survive high temperature manufacturing processes. In the manufacturing of solid oxide fuel cells (SOFCs), this includes materials that are incompatible with other ceramic

components and/or are otherwise unstable at high temperatures, require nanostructuring, or are used as surface coatings to enhance cell performance [3–6]. Additionally, solution infiltration has advantages over typical high temperature ceramic fabrication techniques because the infiltrate material is not an integral part of the structural component, and thus the cell will not crack if the infiltrated material undergoes dimensional changes during cell operation [7–9]. From a manufacturing standpoint, infiltration can be used to eliminate costly multiple sintering steps [3,6]. Combined, these benefits make infiltration methods an attractive complement to high temperature fabrication techniques.

In terms of individual SOFC components, solution infiltration methods have been found to be particularly useful in making high

\* Corresponding author. Tel.: +1 780 710 7997.

E-mail address: [Hanifi@ualberta.ca](mailto:Hanifi@ualberta.ca) (A.R. Hanifi).

performance cathodes because of the high catalytic surface area created, and because a high temperature cathode sintering step can be avoided [10–13]. For the anode, infiltrated ceria-based materials have been used to increase the catalytic surface area for fuel oxidation [14–17]. For anode-supported cells, Cu infiltration has been extensively investigated because it is a coke-tolerant electronic conductor and can be incorporated in large volumes [18].

As a replacement for conventional Ni-ceramic (cermet) SOFC anodes, infiltrated Ni can help to mitigate thermal stress issues arising from the mismatch of the coefficient of thermal expansion between anode materials and the electrolyte [7], and can improve the mechanical strength of the anode support because a much higher YSZ content (lower Ni content) can be used in the anode [19]. Another benefit of Ni infiltration is enhancement of the cell's tolerance to expansion of NiO during oxidation ('redox cycling'). When Ni is infiltrated into a thin YSZ porous layer in metal-supported [8] and electrolyte-supported [9] fuel cells, significant improvement in the redox cycling resistance is reported because a very low content of nano-sized Ni particles (minimum of ca. 9 vol.% coating the pore walls) can still achieve the electronic percolation threshold [20–22]. Unlike the Ni component in standard Ni–YSZ

cermets, the lower amount and better distributed infiltrated Ni is typically not a structural element and thus is not constrained by Ni oxidation volume changes during redox cycling that can transfer stress to the dense electrolyte.

In spite of these advantages, there are certain challenges associated with SOFC anodes constructed using infiltration. These include loss of electronic conductivity due to Cu [23] and Ni sintering [7,8,17,24], excessive build-up of infiltrate materials on the outer surfaces of the porous structure [23], and the large number of infiltration steps needed to incorporate a sufficiently high volume percentage of the electron conducting component [25]. Co-infiltration of other materials has helped to partially stabilize Cu [26,27] and Ni electronic conduction networks [6,17,28]. For example, doped ceria has been shown to improve the electronic conductivity of a Ni-infiltrated anode in reducing atmospheres by forming electronic bridges between unconnected Ni particles [29]. Equally important, the number of infiltration steps can potentially be greatly lowered through the use of specialized methods [3].

Tubular and planar geometries are two of the more well known SOFC configurations currently under investigation. Although power densities are generally higher for planar cells,

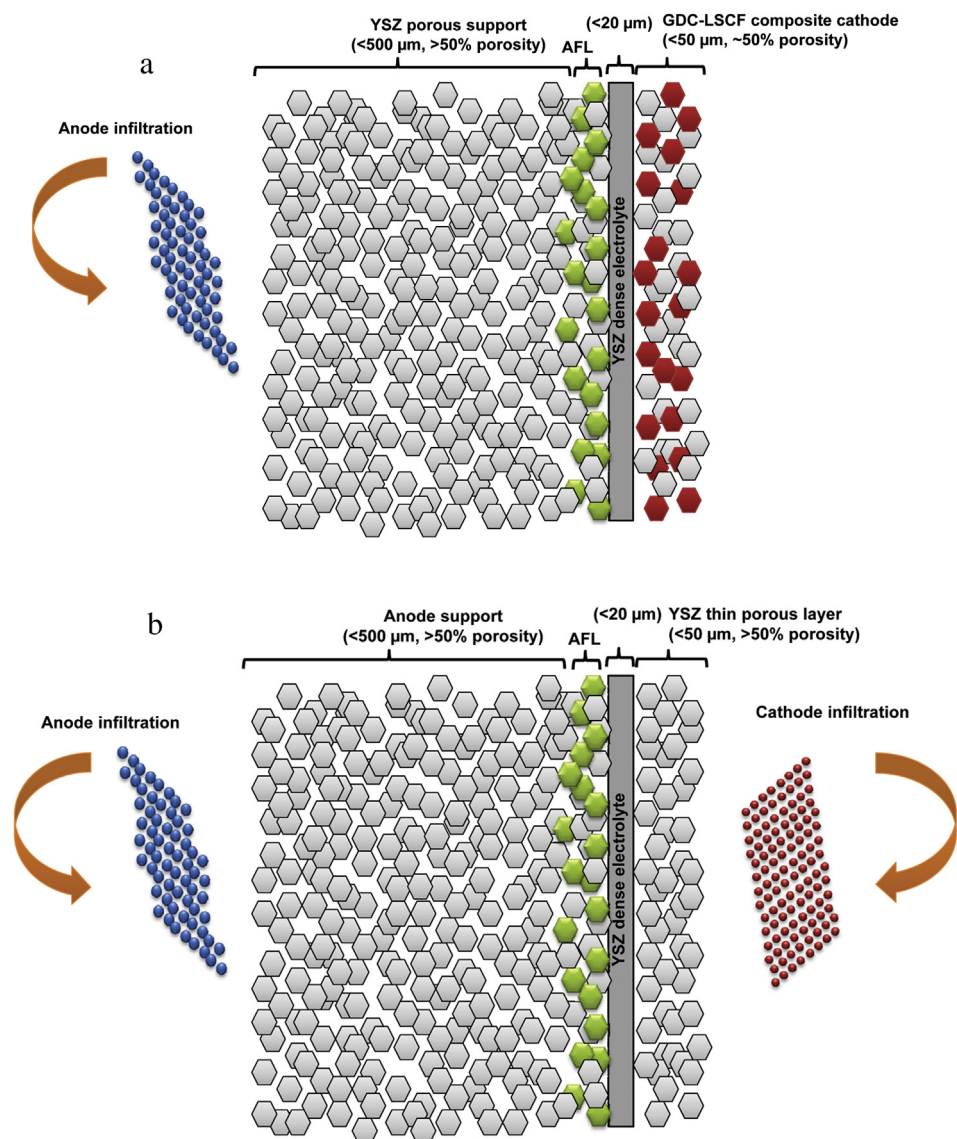


**Fig. 1.** Schematic of a new generation tubular cell with infiltrated anode and a) GDC–LSCF composite cathode, b) LSM infiltrated cathode.

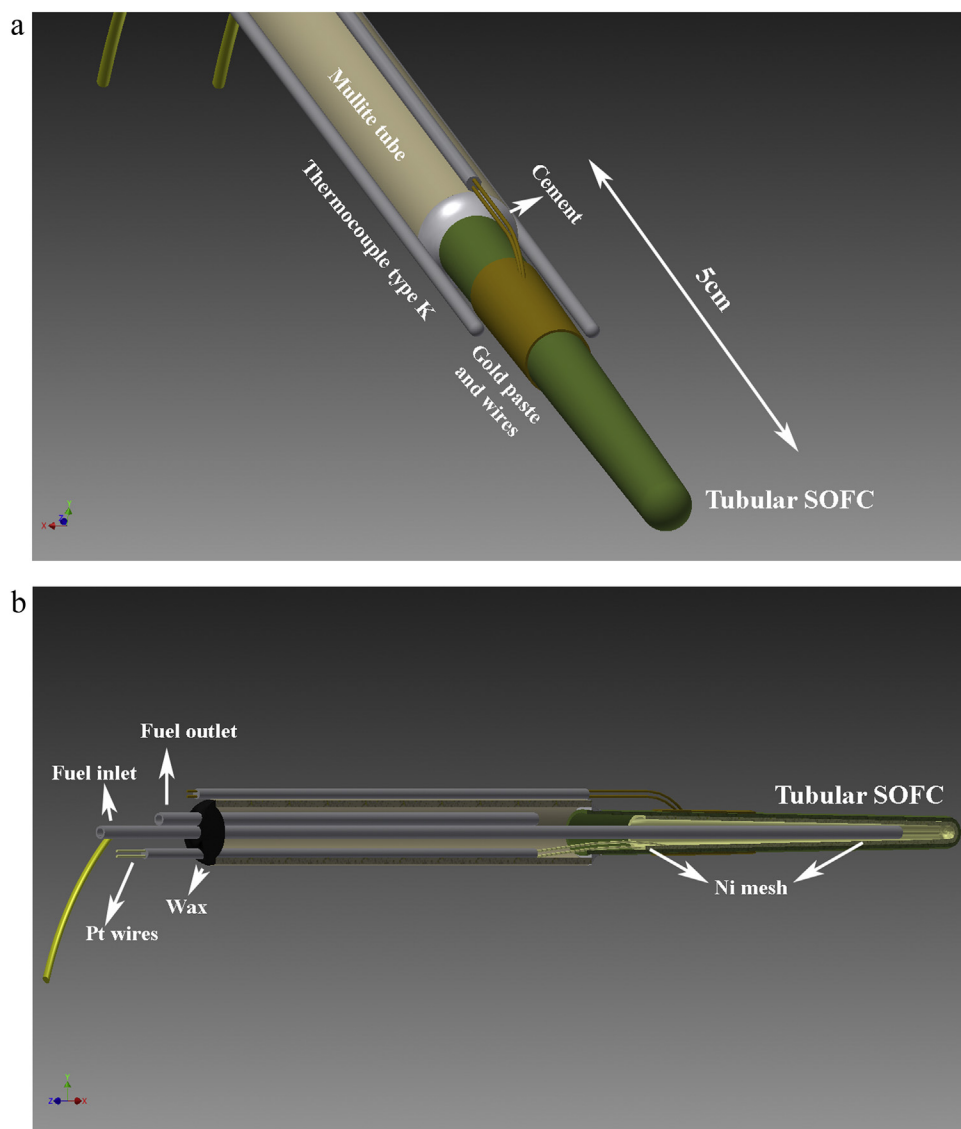


**Fig. 2.** (a) Schematic of the tubular cell, cell holder, thermocouples and cathode leads (b) cross section of the fuel cell showing gas manifolds, sealing and electrodes leads. The furnace heating coils closely surrounded only the fuel cell.

tubular fuel cells have a higher thermal shock resistance, are easier to seal and manifold because the seals can be placed outside the furnace hot zone [30,31], and it is easier to infiltrate materials specifically into either the anode or cathode side of the cell, versus the situation in planar configurations. A third generation of infiltrated tubular SOFCs has recently been developed by the authors to overcome redox cycling problems, typically

associated with anode-supported SOFCs [32,33], based on slip-cast porous YSZ tubes. Because of their high degree of porosity, they exhibit improved thermal and redox cycling tolerance [34,35]. Also, they have been shown to be infiltratable using conventional aqueous solutions [34,35], and a new two-step infiltration process, employing surfactants and complexing agents, using these tubes has recently been reported [36].

The present work explores the use of hot solution (100 °C) infiltration methods in the fabrication of tubular full cells. Specifically, infiltration of NiO–SDC ( $\text{Sm}_{0.2}\text{Ce}_{0.8}\text{O}_{1.9}$ ) is shown here to augment the electronic conduction pathways in two types of cells, one based on porous YSZ and the other on porous NiO–YSZ cermet support structures. These cells used either an LSM (nominally  $\text{La}_{0.8}\text{Sr}_{0.2}\text{MnO}_{3+\delta}$ ) cathode infiltrated into a thin porous YSZ film, or a GDC–LSCF ( $\text{Gd}_{0.1}\text{Ce}_{0.9}\text{O}_{1.95}$ – $\text{La}_{0.6}\text{Sr}_{0.4}\text{Co}_{0.2}\text{Fe}_{0.8}\text{O}_{3-\delta}$ ) composite material as the cathode, respectively. The performance of these cells are compared with the distribution of anode and cathode materials found within each, with the use of GDC–LSCF cathode and the NiO–YSZ cermet support giving roughly 25% better power densities.

**Table 1**  
Compositions used to prepare NiO–SDC and LSM infiltrate solutions.

Infiltrate reagents	NiO–SDC (g) (cells A and B)	LSM (g) (cell B)
$\text{Ni}(\text{NO}_3)_2 \cdot 6\text{H}_2\text{O}$	3.86	—
$\text{Sm}(\text{NO}_3)_3 \cdot 6\text{H}_2\text{O}$	0.34	—
$\text{Ce}(\text{NO}_3)_3 \cdot 6\text{H}_2\text{O}$	1.34	—
$\text{La}(\text{NO}_3)_3 \cdot 6\text{H}_2\text{O}$	—	2.94
$\text{Sr}(\text{NO}_3)_2$	—	0.36
$\text{Mn}(\text{NO}_3)_2 \cdot 4.6\text{H}_2\text{O}$	—	2.23
Water	1.00	1.00
Triton (X-45)	0.30	0.30

**Table 2**  
Components used to prepare cells A and B.

Component	Cell A (mole ratio)	Cell B (mole ratio)
Anode current collector	Ni gauze + NiO paste	Ni gauze + NiO paste
Anode support	Porous 5 wt% NiO:YSZ	Porous YSZ
Anode infiltrate	(3.5:1) Ni:SDC × 35 infiltrations	(3.5:1) Ni:SDC × 15 infiltrations
Anode functional layer	(1:1) Ni:YSZ	(1:1) Ni:YSZ
Electrolyte	ca. 10 μm YSZ + thin GDC cathode-side film	ca. 10 μm YSZ
Cathode	(1:1 wt%) GDC:LSCF	Porous YSZ
Cathode infiltrate	—	"LSM"
Cathode current collector	Au paste	Au paste

## 2. Experimental methods

The slip-casted tubular ceramic SOFCs under investigated here consisted of a porous YSZ support with a ca. 500 μm wall thickness, coated with a thin 50:50 wt% NiO:YSZ anode functional layer, a dense YSZ electrolyte, and a thin porous YSZ. Fig. 1 shows a schematic diagram of this design, where the porous YSZ zones have 50–55% open porosity following sintering. The porous support was produced by casting an aqueous slip composed of calcined YSZ powder, with or without a small amount of added NiO, while the other layers were applied by dip coating, and

eventually modified by infiltration of NiO–SDC (samaria-doped ceria) into the porous support. For the cathode, a GDC–LSCF (gallium-doped ceria–lanthanum strontium cobalt ferrite) composite cathode (Fig. 1a) was compared to a LSM (lanthanum strontium manganite) infiltrated porous YSZ film (Fig. 1b). The tube diameter, length, and active surface area of the fuel cells studied are 6 mm, 5 cm and ~2 cm<sup>2</sup>, respectively (Fig. 2a). The top 1 cm of the tube was used for sealing purposes. For this work, two individual tubes were studied, with their compositions and characteristics detailed in Tables 1 and 2.

### 2.1. Fabrication of the porous YSZ support

Porous support tubes were manufactured according to prior work [32,33]. Briefly, a suitable slip used to cast the infiltrated cell was produced from YSZ powder (TZ-8Y, 8 mol% Y<sub>2</sub>O<sub>3</sub>, Tosoh), calcined at 1500 °C for 3 h and then ball milled with various components, including 0 or 5 wt% NiO (J.T. Baker), 8.6 wt% graphite (20 vol.%) (Sigma Aldrich, <325 mesh), 2% hydrochloric acid (pH 4 adjustment) and water to give 40% suspended solids. To create the tubular support, the slip was cast into a plaster mold for about 1 min, after which the excess slip was quickly poured out. The wet tube was then dried at room temperature for 1 h. The resulting drying facilitates the removal of the as-made YSZ tube. These closed end tubes were dried at 100 °C in an oven, heated at 700 °C for 1 h, and then pre-sintered in air at 1150 °C for 3 h.

### 2.2. Anode functional layer and dense YSZ electrolyte

The electrolyte suspension was prepared by mixing Tosoh YSZ, ethanol and binder (6 wt% ethyl cellulose in terpineol) to a 10% solid loading. The ratio of the prepared binder to ethanol was set at 5%. The slip was mixed for 1 h using a ball mill, and then treated ultrasonically for 5 min in order to remove the entrapped air and disperse the agglomerates before application. The slip was coated onto the pre-sintered tubes by dipping them into the suspension for 5 s and then drying. In order to form a gas-tight electrolyte, the dip-coating procedure was repeated 10 times with a 15 min drying interval between coats. A thin anode functional layer (50:50 wt% NiO:YSZ slurry) was deposited on the porous support using a similar formulation and coating procedure, as described above for the YSZ electrolyte.

Following anode functional layer and electrolyte deposition, each tube was sintered at 1350 °C for 3 h. For Cell A, a thin layer of Gd<sub>0.1</sub>Ce<sub>0.9</sub>O<sub>1.95</sub> (GDC 10-M, Fuelcellmaterials) was coated on the YSZ electrolyte following co-sintering of the AFL and the YSZ electrolyte, using a similar slip formula and dip coating method described for YSZ electrolyte and the cell was again sintered at 1350 °C for 3 h. This layer helped to minimize Sr and La migration between the LSCF cathode and YSZ.

### 2.3. Sintered cathode components

Cell B was coated with a thin porous YSZ layer for cathode infiltration. Calcined YSZ (sintered at 1500 °C, milled for 72 h in water, and then dried) was mixed with 8.6 wt% graphite (20 vol.%), dispersant (Menhaden fish oil), azeotropic solvent (toluene/ethanol), and binder (polyvinyl butyral). The components were mixed at 300 rpm for 1 h in a planetary mill prior to coating. The mixture was then applied to the electrolyte by dip coating once. The tube was heat treated at 300 °C (1 h), 700 °C (1 h) and sintered at 1350 °C for 3 h. For Cell A, a composite GDC–LSCF cathode was prepared using a 50:50 wt% ratio of GDC:LSCF (LSCF-P, Fuelcellmaterials) plus 20 vol.% graphite as the pore former. The tube was dipped once into the slurry, similarly to what was done during

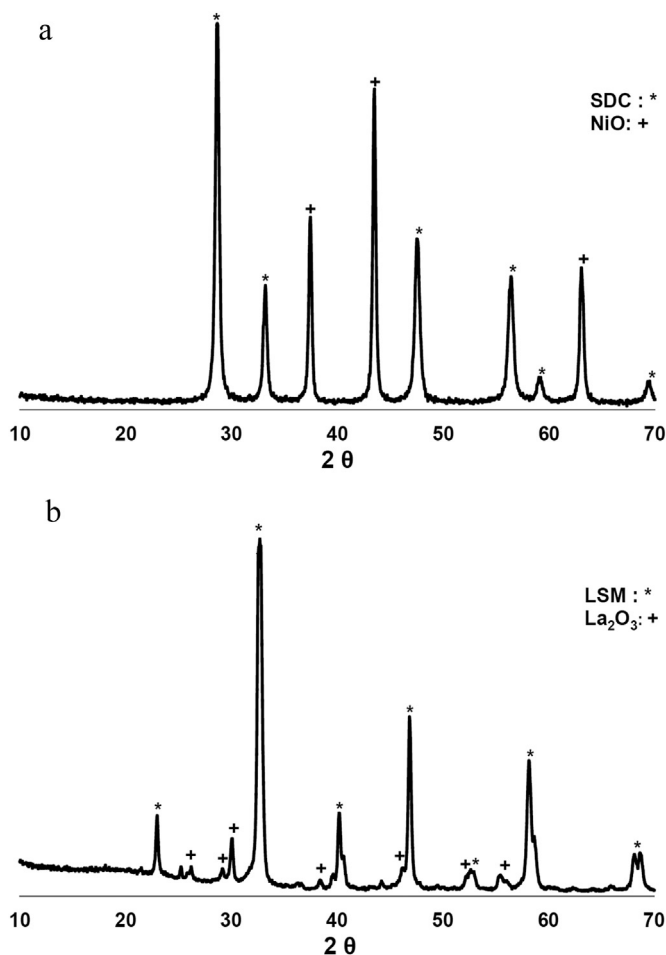


**Fig. 3.** XRD pattern of (a) NiO–SDC phases and (b) LSM phase following heat treatment of their nitrate salts at 700 °C.



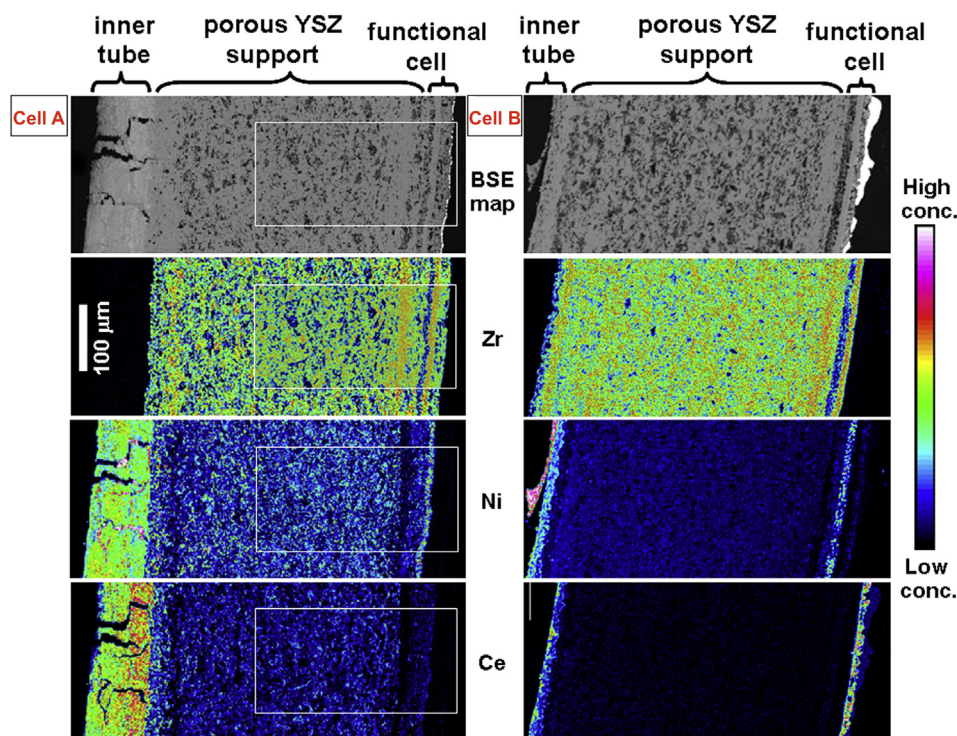


**Fig. 4.** BSE and WDX element maps of the polished cross-sectional structures of cells A (with a GDS–LSCF cathode) and B (with an LSM infiltrated cathode). For Cell A, high resolution maps (outlined in white) overlay the low resolution images. The maps for Cell B are of an intermediate resolution. The color scale gives the relative intensity of a given element in a map, which was expanded to maximize the contrast. Relative intensities cannot be quantitatively compared between maps. (For interpretation of the references to color in this figure legend, the reader is referred to the web version of this article.)

the preparation of the thin porous YSZ layer, and sintered at 1150 °C for 3 h.

#### 2.4. Infiltration of the catalysts

In order to infiltrate NiO–SDC into the porous YSZ supported tube,  $\text{Ni}(\text{NO}_3)_2 \cdot 6\text{H}_2\text{O}$ ,  $\text{Sm}(\text{NO}_3)_3 \cdot 6\text{H}_2\text{O}$  and  $\text{Ce}(\text{NO}_3)_3 \cdot 6\text{H}_2\text{O}$  (Alfa Aesar) were mixed with a small amount of a polymeric dispersant (Triton X-45, Union Carbide Chemicals and Plastics Co. Inc.) and water. The list of reagents and their amounts used for infiltration of NiO–SDC are shown in Table 1. The mixture was heat treated at 100 °C to give a high viscosity, concentrated solution. The tubular cell was preheated to 120 °C, the hot viscous solution was poured inside, and a room temperature vacuum infiltration chamber was used to enhance the penetration of the infiltrate mixture. The excess infiltrate was removed from the tube using a pipette. The tube was then heat treated at 120 °C (15 min) and 350 °C (15 min), followed by a repeat of the infiltration process. For Cell A, the infiltration procedure was repeated 35 times, giving a 43 wt% increase, while Cell B was infiltrated 15 times, giving a 25 wt% increase. An infiltrate solution was also heated to 700 °C in air for 1 h, and used for the x-ray diffraction (XRD) analysis studies.

For Cell B, the LSM infiltrate solution was prepared by mixing appropriate amounts of  $\text{La}(\text{NO}_3)_3 \cdot 6\text{H}_2\text{O}$  (Alfa Aesar),  $\text{Sr}(\text{NO}_3)_2$  (Alfa Aesar),  $\text{Mn}(\text{NO}_3)_2 \cdot x\text{H}_2\text{O}$  ( $x = 4.6$  calculated) (Aldrich), Triton X-45, and water (Table 1). The mixture was infiltrated twice into the thin porous YSZ layer using a procedure similar to the one discussed above for NiO–SDC. In this manner, roughly 30 wt% LSM was infiltrated into the 50% porous YSZ layer. An infiltrate solution was also heated to 700 °C in air for 1 h and used for the x-ray diffraction (XRD) analysis studies.

#### 2.5. Fuel cell set-up and electrochemical performance testing

Fig. 2 (a and b) shows a general scheme of the fuel cell test set-up used in this work, while Table 2 lists the characteristics of each cell studied. A rolled Ni mesh current collector (Alfa Aesar) brushed with NiO paste (binder: 6 wt% ethyl cellulose in terpineol and solvent: ethanol) was tightly pushed inside the tube to ensure good contact with the anode wall. Gold paste and coiled Au wires were used as the cathode current collector. The tubular cell was attached to a mullite support tube using Ceramabond 552-VFG/thinner (Aremco, NY). Once assembled, only the tubular cell was placed in a micro furnace, such that the mullite–Ceramabond contact was just on the edge of the hot zone. Two thermocouples placed next to the cathode on opposite sides of the tubular cell were used to monitor the temperature. 50 mL min<sup>−1</sup> N<sub>2</sub> was fed inside the tube via a stainless steel needle during temperature ramp up and chemical conversion of the infiltrate components. When the cell reached 800 °C, the anode was gradually reduced as the fuel gas was switched from N<sub>2</sub> to humidified H<sub>2</sub> (3 vol.% H<sub>2</sub>O) in 5 mL min<sup>−1</sup> increments every 15 min, keeping the total gas flow at 50 mL min<sup>−1</sup> over the 2.5 h period. Air flowed over the cathode was 50 mL min<sup>−1</sup>. Open circuit potential (OCP), *E*–*I* measurements, electrochemical ac impedance spectroscopy (EIS), and potentiostatic analyses were carried out with a four probe configuration using a Solartron 1287/1255. The ca. 2 cm<sup>2</sup> cathode area was used to define the cell current and power density.

#### 2.6. Post electrochemical analyses

Following cell testing, both fractured and well-polished pieces (down to 1 μm diamond paste) of each cell were studied by scanning electron microscopy (JEOL 6301F) and electron microprobe

(JEOL JXA-8200). The volume percentage (vol.%) of pores was calculated based on the area fraction of surface pores on the polished samples, as determined from processed scanning electron backscattered electron (SEM BSE) images taken at 100–200 $\times$  resolution. Electron microprobe WDX element maps and quantitative elemental analyses were performed on polished and carbon-coated samples. Internal inorganic standards were used to calibrate the band location and signal intensity of each element. WDX quantitative analysis results for each element and sample were based on the average signal taken from 51 random data analysis points within a given region (taken over a 250  $\mu\text{m}$  distance). These results were converted to vol.% data using the pore area percentage determined from the BSE images and densities of 8YSZ, Ni and  $\text{CeO}_2$  of 5.6 g  $\text{cm}^{-3}$ , 8.90 g  $\text{cm}^{-3}$  and 7.132 g  $\text{cm}^{-3}$ , respectively.

### 3. Results and discussion

The primary goal of this work is to manufacture high performance tubular SOFCs using simple, inexpensive methods. This is being achieved by the incorporation of anode and cathode catalysts, as well as electronically conducting components, into porous YSZ support structures using the hot solution infiltration method. To achieve these objectives, slurries of calcined/ball-milled Tosoh

YSZ powder were used to form the slip cast porous YSZ support structure [32–34,37]. The enlarged YSZ particles lead to a less dense YSZ structure after 1350  $^{\circ}\text{C}$  sintering, and thus a larger pore volume and surface area due to a larger number of small (<1 micron) interconnected pores within the sintered porous YSZ architecture [38]. A thin, co-fired NiO–YSZ anode functional layer (AFL) was deposited on the porous YSZ support before coating it with YSZ electrolyte in order to both increase anode catalytic performance and to simplify the deposition of a uniformly dense electrolyte layer. The logic behind this was that this fine particulate AFL could serve to remove surface irregularities on the ‘green’ (as formed) slip-cast YSZ tube surface. As well, NiO may serve as a sintering aid for the formation of the dense electrolyte film [39,40].

The thin, dip-coated porous YSZ layer on the electrolyte layer was then co-fired in Cell B in order to subsequently deposit the cathode architecture (Table 2). A similar approach has been shown to improve the electrochemical performance of LSM [38] and LSBT [41] cathodes. The anode and cathode components were then independently deposited using multiple infiltration steps, employing hot (close to 100  $^{\circ}\text{C}$ ) solutions containing the metal precursors. Due to the ca. 0.5 mm thickness of the porous YSZ tubular support (anode) relative to the ca. 10  $\mu\text{m}$  porous YSZ layer used for the cathode, it was more important that the anode

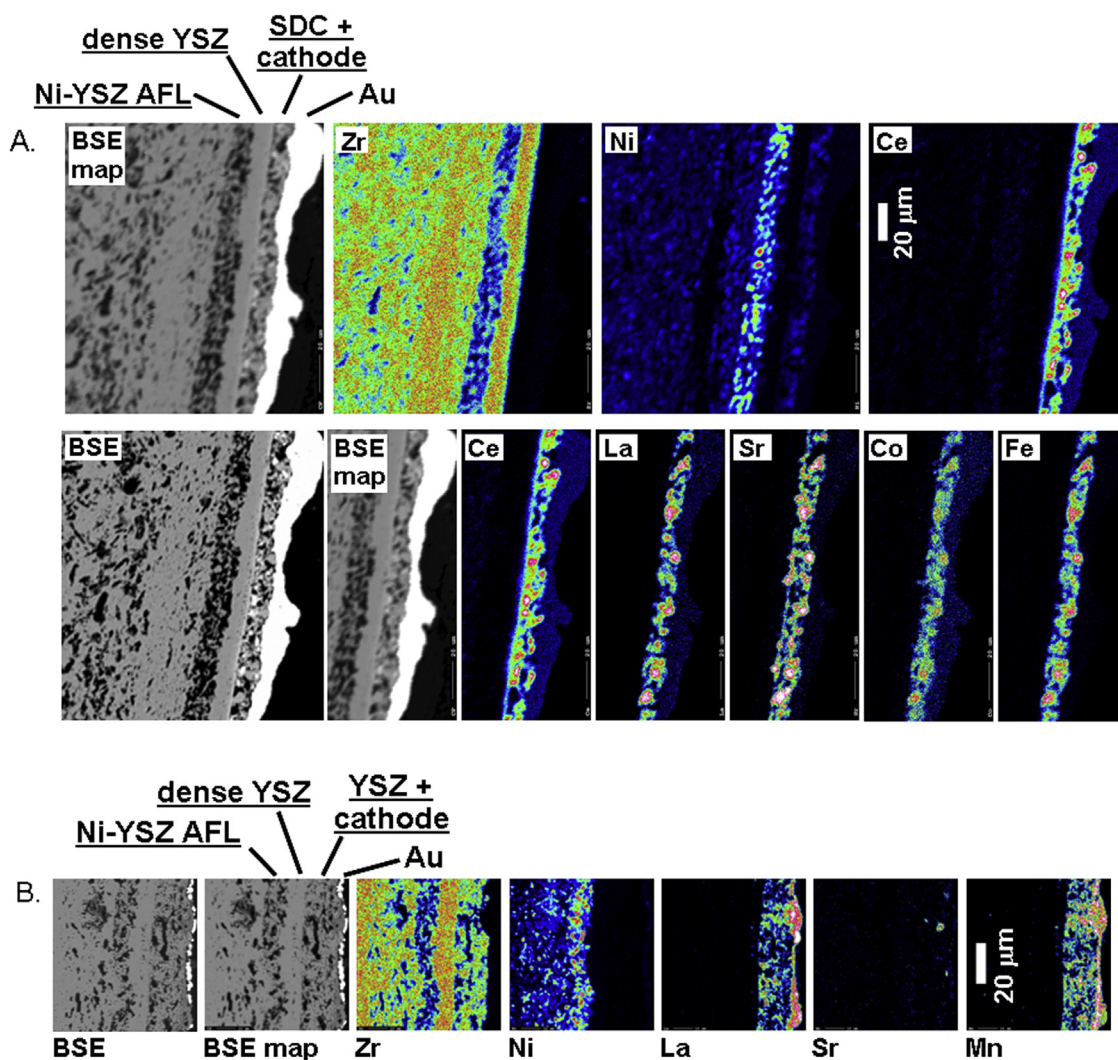


**Fig. 5.** SEM BSE and high resolution WDX element maps of the polished cross-section structures of (a) Cell A and (b) Cell B. BSE mapped images are reproduced within each element map. Standard SEM BSE and mapped BSE images are compared side-by-side to show where small, instrument-based artifacts occurred in the maps.



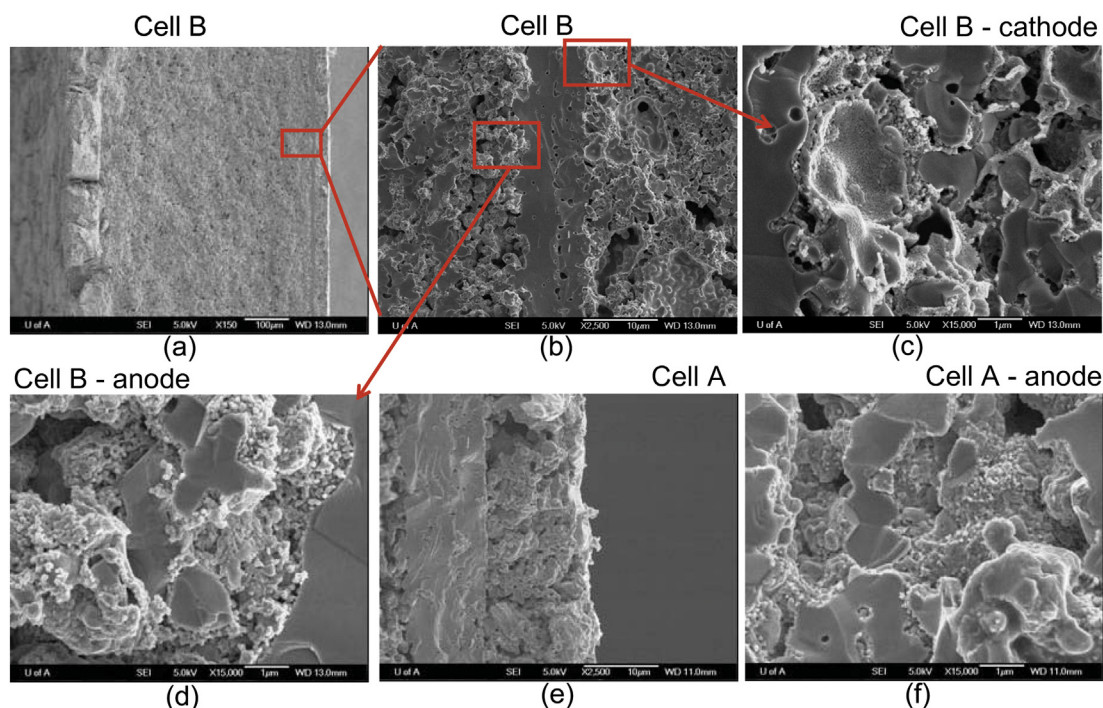


**Fig. 6.** SEM images of (a) cross-section of Cell B, (b) Cell B anode, electrolyte and cathode interfaces, (c) LSM infiltrated porous YSZ cathode of Cell B, (d) Ni–SDC infiltrated Ni–YSZ anode functional layer of Cell B, (e) Cell A anode, electrolyte and GDC–LSCF composite cathode interfaces, (f) Ni–SDC infiltrated Ni–YSZ anode functional layer of Cell A.

infiltrate achieve the high electronic conductivity offered by Ni, while the emphasis for the cathode was on high catalytic activity. In this study (Table 2), Cell A and Cell B contained 5 and 0 wt% NiO, respectively, in their slip-casted structure, and then both were further hot-infiltrated with NiO–SDC. For the cathode, Cell B was infiltrated with LSM, while Cell A had a GDC–LSCF composite cathode. The formation of two phases, following heat treatment of the NiO and SDC components at 700 °C, was confirmed from their XRD pattern (Fig. 3a). A similar heat treatment and XRD analysis of the LSM infiltrate solution showed small amounts of unreacted  $\text{La}_2\text{O}_3$  in the cathode (Fig. 3b).

### 3.1. Microstructural analysis

In this work, macroscopic and microscopic analyses were performed on both freshly reduced and electrochemically tested cells

in order to determine the distribution of the infiltrated materials within the cathode and anode layers. Fig. 4 shows the back-scattered electron SEM image and representative WDX map distributions of Zr, Ni and Ce, acquired across the polished cross-sections of cells A and B. WDX map analysis for Sm (not shown), performed for Cell B, showed a significantly lower Sm content with grading that matched the Ce.

What is immediately apparent from Fig. 4 is that Cell A has both a better distribution and a higher concentration of Ni and Ce within the 0.4–0.5 mm thick, porous YSZ support structure, and a very thick film of inorganic material (ca. 100  $\mu\text{m}$ ) coating the inner portion of the porous YSZ tube. This film contains many cracks that are partially filled with excess Ni, perhaps resulting from phase separation from the bulk material during reduction in  $\text{H}_2$ . In contrast, the inner tube film found for Cell B is quite thin (Fig. 4). Note that regions of high Ni content on the left side of this film show the location of the NiO paste current collector.

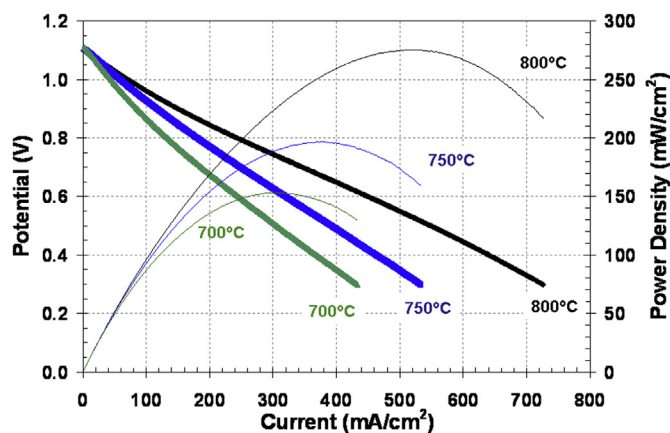


**Fig. 7.** Electrochemical performance of Cell A as a function of temperature. Anode: 50 mL min<sup>-1</sup>  $\text{H}_2$  (3%  $\text{H}_2\text{O}$ ). Cathode: 50 mL min<sup>-1</sup> air. Current scan rate: 3.3 mA s<sup>-1</sup>.

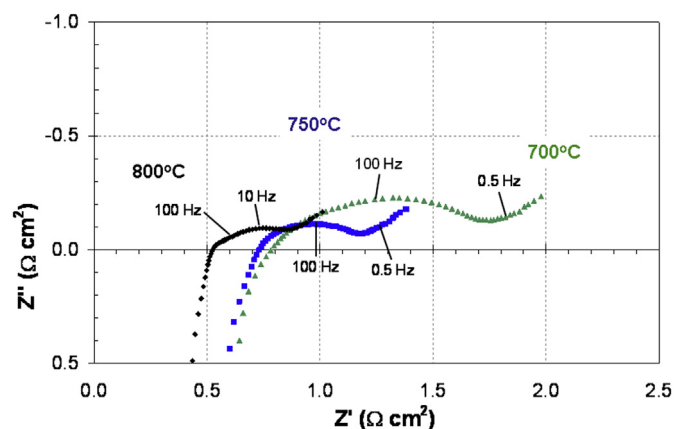


**Fig. 8.** EIS Nyquist plot of Cell A as a function of temperature. DC bias: open circuit potential, AC bias:  $\pm 10$  mV rms, frequency range: 100 kHz–0.1 Hz.

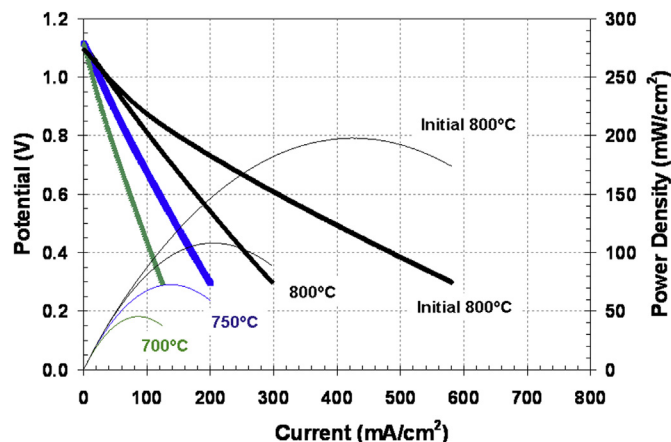


**Fig. 9.** Electrochemical performance of Cell B as a function of temperature. Anode: 50 mL min<sup>-1</sup> H<sub>2</sub> (3% H<sub>2</sub>O). Cathode: 50 mL min<sup>-1</sup> air. Current scan rate: 3.3 mA s<sup>-1</sup>. The “initial 800 °C” data set was acquired soon after the electrochemical study was initiated at 800 °C. The remaining data were acquired six days later following long term stability testing at an applied cell potential of 0.7 V and 800 °C (see Fig. 10).

Within the porous YSZ support, the element maps of Cell B (Fig. 4), in particular, show a varying Ni and Ce content, graded from high amounts at the inner tube surface to quite low next to the Ni–YSZ anode functional layer. Based on the original targeted 50 vol.% YSZ found in the porous YSZ and 5 wt% NiO–YSZ support structures and WDX quantitative spot analyses located roughly in the center of the anode support layer of the two cells in Fig. 4, Cell A is found to have 37 vol.% pores, 10 vol.% Ni, 50 vol.% YSZ and 3 vol.% SDC, while cell B contains 45 vol.% pores, 4 vol.% Ni, 50 vol.% YSZ and 1 vol.% SDC. This suggests that the porosity of the anode support for both cells is sufficient for gas transport, but it remains unclear from Fig. 4 whether the ca. 100 μm thick Ni–SDC inner tube film would inhibit gas access to the anode. In addition, the amount of Ni within the porous support is at or below the 9 vol.% percolation threshold limit for finely distributed Ni particles [21], which raises concerns as to whether the support, especially for Cell B, has sufficient electronic conductivity to perform well as a fuel cell.

Differences seen on the anode side of the cell in Fig. 4 result from the pre-incorporation of 5 wt% NiO in the support structure and the number of hot solution infiltration steps used (35 times vs. 15 times) in the construction of the two cells. As seen, the larger number of infiltration steps can lead to a thick inner tube film

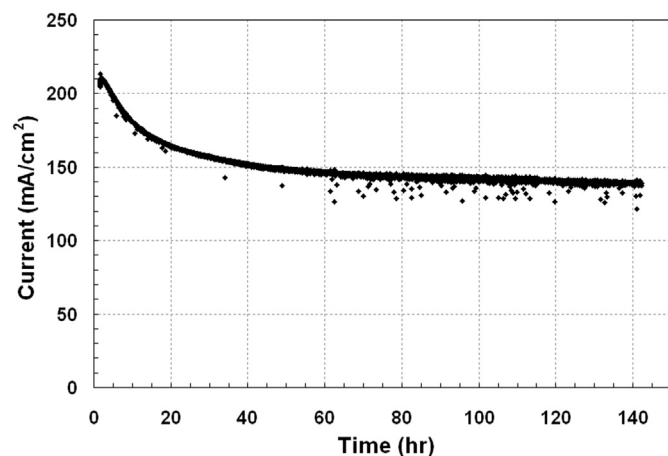


**Fig. 10.** Electrochemical performance of Cell B over time. Anode: 50 mL min<sup>-1</sup> H<sub>2</sub> (3% H<sub>2</sub>O). Cathode: 50 mL min<sup>-1</sup> air. 0.70 V cell potential.

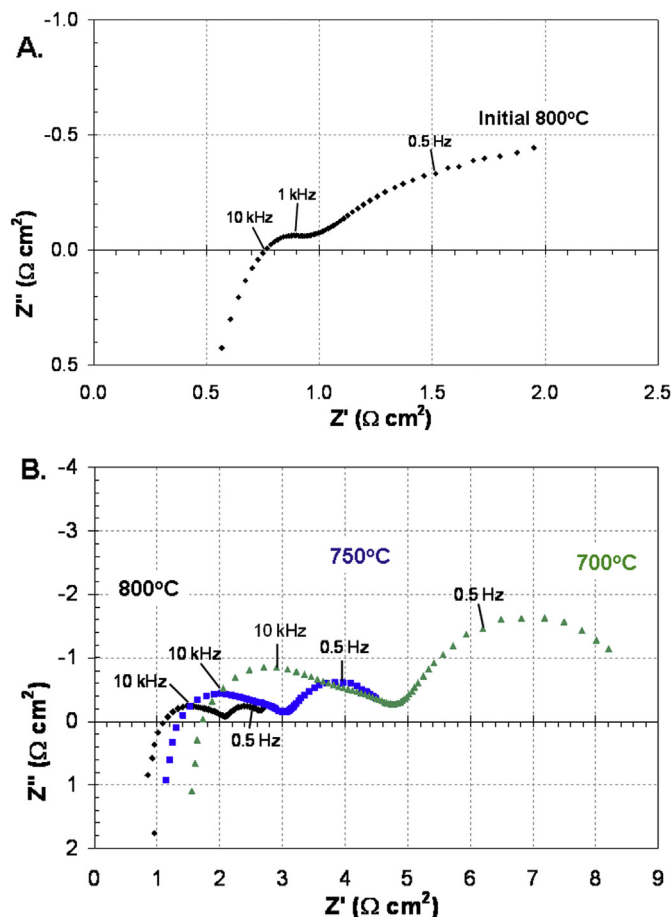


**Fig. 11.** EIS Nyquist plot of Cell B as a function of temperature. (a) The “initial 800 °C” data set was acquired soon after the electrochemical study was initiated at 800 °C. (b) EIS data acquired six days later following the long term stability testing (see Fig. 10). DC bias: open circuit potential, AC bias: ±10 mV rms, frequency range: 100 kHz–0.1 Hz.

enriched in the Ni and Ce components, and alternatives are offered in the literature to minimize this problem [23]. Even so, quantitative WDX analysis within the middle of the porous YSZ support in Fig. 4 clearly shows that significant Ni and Ce content exist. Even more important, when the maps in Fig. 4 are set at a far higher contrast (not shown), Ni and Ce were found in all of the resolvable pores within the porous YSZ support. This demonstrates that hot solution infiltration serves to penetrate even regions that seem to be blocked by relatively dense zones of YSZ, formed during the slip-casting fabrication process employed.

A closer analysis of the tubular cells reveals a well-defined anode functional layer (AFL), a dense YSZ electrolyte, and a uniform and well-constructed cathode layer. Fig. 5 shows higher magnification SEM BSE images and representative WDX map distributions of Zr, Ni, Ce, La, Sr, Mn, Fe, and Co across one small portion of the polished cross-sections of cells A and B. The thickness of the various layers does change by up to 100% between locations in some areas, but the layers generally have the same morphology as shown in Fig. 5, and all the layers are seen to be intact.

The Ni content of the AFL is qualitatively similar for cells A and B, but significantly higher than that found in the porous YSZ support. The dense YSZ film is observed to be quite uniform and relatively defect-free in both cells. For Cell A (Fig. 5a), the dense YSZ electrolyte is coated with a dense, ca. 1 μm thick Ce-containing film that is likely a YSZ-modified GDC material, formed at the 1350 °C sintering temperature employed. For both cells, the cathode



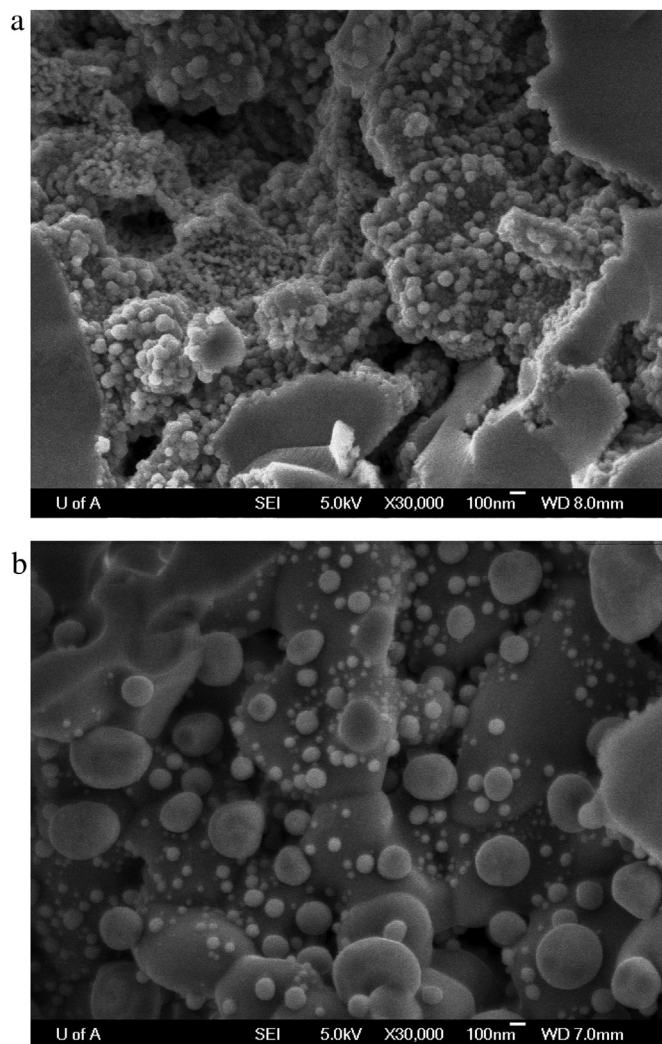


**Fig. 12.** SEM images showing the microstructure of infiltrated porous YSZ support structures (a) within the Ni–SDC infiltrated porous YSZ anode support in Cell A, and (b) within the middle of a typical Ni infiltrated porous YSZ support.

components are found primarily in relatively large pockets. However, in a few locations within the cathode of Cell B (Fig. 5B), relatively low levels of Sr were seen, suggesting the presence of some lower doped lanthanum manganite cathode in these regions. The low resolution of the electron microprobe method prevents us from identifying single phases, as the technique cannot resolve particles much less than 1  $\mu\text{m}$  in diameter. However, it can be clearly seen that hot infiltration has led to a build-up of infiltrate material on the outer cathode surface of both cells, indicating that the infiltrate content inside the porous YSZ cathode will also be somewhat lower than anticipated.

To better resolve the size and distribution of the hot-infiltrated components following electrochemical testing, a series of high resolution SEM images were acquired using broken cell pieces. For Cell B (Fig. 6a, from left to right) is found a thick inner tube film, a ca. 550  $\mu\text{m}$  thick infiltrated porous YSZ support, and the various other cell components. Closer inspection of Cell B (Fig. 6b) reveals, from left to right, a small section of the anode support, the functional anode layer, the YSZ electrolyte film (ca. 9  $\mu\text{m}$  thick), and a portion of the ca. 28  $\mu\text{m}$  thick porous YSZ–LSM infiltrated cathode. At even higher magnification, Fig. 6c shows the fine distribution of well inter-connected 50–100 nm LSM particles on the YSZ pore

walls next to the electrolyte of Cell B. These small LSM particles should give a high catalytic surface area and a well-connected current pathway [42,43]. In Fig. 6d, the Ni–YSZ cermet particles in the anode, next to the YSZ electrolyte layer, are covered by what appears to be Ni and SDC nanoparticles.

For comparison, the interfaces of the anode functional layer, the ca. 12  $\mu\text{m}$  YSZ electrolyte layer, and the ca. 14  $\mu\text{m}$  GDC–LSCF cathode of Cell A are seen in Fig. 6e. Similar to Cell B, Cell A (Fig. 6f) also shows the presence of fine Ni–SDC infiltrate particles in the AFL layer.

### 3.2. Fuel cell performance

Three major differences are present for cells A and B, including the thickness of thick inner tube film, the amount of Ni and Ce found within the porous YSZ support, and the type of cathode employed. Fig. 7 shows the cell potential versus current density, as well as the power curves, for Cell A. The cell exhibited an open circuit potential of 1.099 V (800  $^{\circ}\text{C}$ ), 1.106 V (750  $^{\circ}\text{C}$ ), and 1.114 V (700  $^{\circ}\text{C}$ ), which are all quite high values, indicating no leakage of air and fuel between the cathode and anode compartments in Cell A, respectively.

Peak power outputs for Cell A of 275  $\text{mW cm}^{-2}$  (800  $^{\circ}\text{C}$ , 0.525 V), 196  $\text{mW cm}^{-2}$  (750  $^{\circ}\text{C}$ , 0.523 V), and 153  $\text{mW cm}^{-2}$  (700  $^{\circ}\text{C}$ , 0.513 V) are seen in Fig. 7, with the primary source of loss being the ohmic resistance of the cell. As shown in Fig. 8, the high frequency ohmic resistance portion of the electrochemical impedance (EIS) of Cell A ranges from 0.5 to 0.8  $\Omega \text{ cm}^2$ . Depending on the method of manufacture, dense, 10  $\mu\text{m}$  thick 8YSZ electrolyte films should not contribute much more than 0.1  $\Omega \text{ cm}^2$  of resistance in this temperature range [based on a 0.03  $\text{S cm}^{-1}$  conductivity at 800  $^{\circ}\text{C}$  and 0.02 at 700  $^{\circ}\text{C}$  [44]. Thus, other losses, such as current collectors and electronic conduction through the porous YSZ support, must be the source of this resistance in Cell A.

The high to mid-frequency portion of the EIS response for Cell A in Fig. 8 is dominated by multiple overlapping arcs (0.4–1.0  $\Omega \text{ cm}^2$ ) that increase in resistance and evolve in shape with decreasing temperature. At this point, we have not been able to conclusively correlate the various individual anode and cathode processes with each EIS arc [45]. However, the low frequency arc, with a peak frequency at below 0.1 Hz (Fig. 8), may be attributed to gas/surface transport restrictions within the current collector-cell assembly [45,46]. Restricted gas flow could be expected for Cell A, considering its relatively thick Ni–SDC inner tube film (Fig. 4).

As compared to Cell A, Cell B has a far thinner Ni–SDC inner tube film (Fig. 4), a lower volume percentage of Ni and Ce within the porous YSZ support layer, and a different cathode material. The impact of those changes on the cell performance is seen in Fig. 9. Even with a good open circuit potential of 1.094 V (800  $^{\circ}\text{C}$ ), Cell B produced a lower initial peak power output of 198  $\text{mW cm}^{-2}$  (Fig. 9, “Initial 800  $^{\circ}\text{C}$ ” data) than Cell A (275  $\text{mW cm}^{-2}$ , Fig. 7). Although the cathode could be the primary cause of the poorer cell performance of Cell B, other tubular cells constructed with 50:50 Ni–YSZ cermet anode support structures and similar cathode configurations produced in the authors’ lab (data not shown), generated peak power outputs of ca. 600  $\text{mW cm}^{-2}$  at 800  $^{\circ}\text{C}$ . Thus, it would seem that factors other than cathode performance are leading to the initially poor performance of Cell B.

To determine the long term performance of these types of cells, Cell B was monitored at 800  $^{\circ}\text{C}$  over 6 days at a 0.70 V cell potential (Fig. 10). An initial rapid decay in current density over the first 40 h was followed by a slow, steady decay of ca. 8% per 100 h, giving an overall decay of 32%. This is reflected in the subsequent power curves (Fig. 9), where the open circuit potentials remained good (1.108 V at 800  $^{\circ}\text{C}$ , 1.114 V at 750  $^{\circ}\text{C}$ , and 1.114 V at 700  $^{\circ}\text{C}$ ), but the

peak power densities had dropped by ca. 45% at 800 °C (108 mW cm<sup>-2</sup> at 800 °C, 0.528 V; 73 mW cm<sup>-2</sup> at 750 °C, 0.529 V; and 45 mW cm<sup>-2</sup> at 700 °C, 0.525 V). This drop in performance possibly arises from a loss in the electronic conductivity within the porous anode support, in a similar manner observed for Ni-infiltrated porous YSZ monoliths by Klemenso et al. [17]. In that work, higher Ni and Ce loadings tended to lead to a less severe loss of electronic conductivity over time.

This loss in performance is also observed in the impedance data as an increase in ohmic resistance. The initial EIS data, collected at 800 °C (Fig. 11a) immediately before the Cell B degradation study, gave a ca. 0.75 Ω cm<sup>2</sup> ohmic resistance, a value that is significantly higher than the 0.52 Ω cm<sup>2</sup> observed for Cell A, and consistent with the lower loading of Ni within the porous YSZ support (Fig. 4). After 6 days at 0.7 V, the ohmic resistance from EIS data taken at 800 °C rose to ca. 1.1 Ω cm<sup>2</sup> (Fig. 11b), a 32% increase from 0.75 Ω cm<sup>2</sup>. Because all EIS determined resistances are larger at 800 °C in Fig. 11b, it would seem that loss of ohmic conductivity through the porous YSZ support leads to direct loss of anode activity, perhaps through disconnected electronic pathways to isolated reaction sites within the anode functional layer. Interestingly, because the resistance of the low frequency arc for Cell B in Fig. 11b increases with decreasing temperature, it is surmised that the low frequency region is dominated by charge transfer resistance rather than mass transport resistance [45,46]. This is consistent with Cell B having a thin Ni–SDC inner tube film (Fig. 4) that is less likely to impede gas transport.

It remains uncertain why Cell B gives an appreciable cell performance when the roughly 4 vol.% Ni content (in the porous YSZ support) is lower than the ca. 9 vol.% required to reach the electronic percolation threshold when nano-sized Ni particles are used to coat pore walls [20,21]. One possible explanation is that the Ni–YSZ AFL has very good lateral conductivity, allowing reasonable access to much of the triple-phase boundary region next to the dense YSZ electrolyte film. Also, the infiltrated SDC must provide additional electronic pathways between the Ni particles in the porous YSZ support.

In support of this argument, Fig. 12 compares high magnification SEM images obtained from a zone within the porous YSZ support for Cell A (Fig. 12a, 35× Ni–SDC infiltrated) with a porous YSZ support infiltrated solely with Ni (Fig. 12b, 35× Ni infiltrated). It is seen that co-infiltration of SDC controls Ni particle coarsening (Fig. 12a), while without SDC, the spherical, 100–500 nm Ni particles seem more isolated (Fig. 12b), and thus are likely less electronically interconnected. Thus, the infiltrated SDC likely electronically bridges disconnected Ni particles, since doped ceria shows significant electronic conductivity under a reducing atmosphere [29]. Because the particles on the YSZ surface are considerably larger in Fig. 12b compared to 12a, it is also possible that the added SDC also inhibits Ni sintering. Thus, it would seem that SDC plays a far larger role than increasing anode activity towards hydrogen oxidation.

#### 4. Conclusions

This paper shows for the first time the use of hot infiltration as a method to incorporate electrode components into redox cycle tolerant SOFCs based on a porous tubular YSZ substrate design. Here, the performance of two tubular SOFCs, constructed by the hot infiltration of various anode and cathode materials into these porous YSZ substrates, was correlated with detailed post-testing microscopic analysis of the distribution of infiltrated materials within the cells. Infiltrated anode and cathode components were found in all of the resolvable pores within both the porous YSZ support, and the porous cathode structure, showing that hot

solution infiltration serves to penetrate deep and less accessible regions of the pore structure. This technique, developed to maximize the level of incorporated anode and cathode component, must be carefully employed to guard against the build-up of inorganic materials along the surfaces of the porous tube. In terms of cell performance, large through thickness distribution of the anode infiltrate materials, as shown by careful electron microprobe WDX mapping of cell cross-sections, impact anode resistance and stability at low infiltrate levels, and perhaps gas transport at high infiltrate levels. Low levels of Ni and SDC infiltrate can be partially compensated for by the presence of a high performance anode functional layer with good electronic conductivity, and the addition of 5 wt% NiO as a cermet within the porous YSZ support. The relatively good performance of the cells can also be ascribed to the use of ceria in the anode layer, which both stabilizes and electronically interconnects the Ni particles.

#### Acknowledgments

This research was supported through funding to the NSERC Solid Oxide Fuel Cell Canada Strategic Research Network from the Natural Sciences and Engineering Research Council (NSERC) and other sponsors listed at [www.sofccanada.com](http://www.sofccanada.com). We would also like to acknowledge Dr. Rob Marr at the University of Calgary Laboratory for Electron Microbeam Analysis (UCLEMA) for assistance with the electron microprobe analyses.

#### References

- [1] D.R. Rolison, J.W. Long, J.C. Lytle, A.E. Fischer, C.P. Rhodes, T.M. McEvoy, M.E. Bourgar, A.M. Lubers, *Chem. Soc. Rev.* 38 (2009) 226.
- [2] H.S. Liu, C.J. Song, L. Zhang, J.J. Zhang, H.J. Wang, D.P. Wilkinson, *J. Power Sources* 155 (2006) 95.
- [3] T.Z. Sholklapper, C.P. Jacobson, S.J. Visco, L.C. De Jonghe, *Fuel Cells* 8 (2008) 303.
- [4] S.P. Jiang, *Int. J. Hydrogen Energy* 37 (2012) 449.
- [5] R.J. Gorte, J.M. Vohs, *Curr. Opin. Colloid Interface Sci.* 14 (2009) 236.
- [6] S.P. Jiang, *Mater. Sci. Eng. A Struct. Mater. Prop. Microstruct. Process.* 418 (2006) 199.
- [7] C.H. Law, S.W. Sofie, *J. Electrochem. Soc.* 158 (2011) B1137.
- [8] M.C. Tucker, G.Y. Lau, C.P. Jacobson, L.C. DeJonghe, S.J. Visco, *J. Power Sources* 171 (2007) 477.
- [9] A. Buyukaksoy, V. Petrovsky, F. Dogan, *J. Electrochem. Soc.* 159 (2012) B232.
- [10] M. Shah, S.A. Barnett, *Solid State Ionics* 179 (2008) 2059.
- [11] Y. Huang, J.M. Vohs, R.J. Gorte, *Electrochem. Solid-State Lett.* 9 (2006) A237.
- [12] J.M. Vohs, R.J. Gorte, *Adv. Mater.* 21 (2009) 943.
- [13] Z.Y. Jiang, C.R. Xia, F.L. Chen, *Electrochim. Acta* 55 (2010) 3595.
- [14] T.Z. Sholklapper, H. Kurokawa, C.P. Jacobson, S.J. Visco, L.C. De Jonghe, *Nano Lett.* 7 (2007) 2136.
- [15] J.S. Qiao, K.N. Sun, N.Q. Zhang, B. Sun, J.R. Kong, D.R. Zhou, *J. Power Sources* 169 (2007) 253.
- [16] S.P. Jiang, S. Zhang, Y.D. Zhen, A.P. Koh, *Electrochem. Solid-State Lett.* 7 (2004) A282.
- [17] T. Klemenso, K. Thyden, M. Chen, H.-J. Wang, *J. Power Sources* 195 (2010) 7295.
- [18] S. Park, R.J. Gorte, J.M. Vohs, *Appl. Catal. A Gen.* 200 (2000) 55.
- [19] J.R. Wilson, S.A. Barnett, *Electrochem. Solid-State Lett.* 11 (2008) B181.
- [20] S.F. Corbin, X. Qiao, *J. Am. Ceram. Soc.* 86 (2003) 401.
- [21] R.M.C. Clemmer, S.F. Corbin, *Solid State Ionics* 180 (2009) 721.
- [22] D.W. Dees, T.D. Claar, T.E. Easler, D.C. Fee, F.C. Mrazek, *J. Electrochem. Soc.* 134 (1987) 2141.
- [23] S.W. Jung, C. Lu, H.P. He, K.Y. Ahn, R.J. Gorte, J.M. Vohs, *J. Power Sources* 154 (2006) 42.
- [24] T. Klemenso, M. Mogensen, *J. Am. Ceram. Soc.* 90 (2007) 3582.
- [25] S.W. Jung, J.M. Vohs, R.J. Gorte, *J. Electrochem. Soc.* 154 (2007) B1270.
- [26] M.D. Gross, J.M. Vohs, R.J. Gorte, *J. Electrochem. Soc.* 153 (2006) A1386.
- [27] M.D. Gross, J.M. Vohs, R.J. Gorte, *Electrochim. Acta* 52 (2007) 1951.
- [28] S.P. Jiang, Y.Y. Duan, J.G. Love, *J. Electrochem. Soc.* 149 (2002) A1175.
- [29] M. Mogensen, N.M. Sammes, G.A. Tompsett, *Solid State Ionics* 129 (2000) 63.
- [30] K. Kendall, *Int. J. Appl. Ceram. Technol.* 7 (2010) 1.
- [31] K.S. Howe, G.J. Thompson, K. Kendall, *J. Power Sources* 196 (2011) 1677.
- [32] A.R. Hanifi, A. Torabi, T.H. Etsell, L. Yamarte, P. Sarkar, *Solid State Ionics* 192 (2011) 368.
- [33] A.R. Hanifi, A. Torabi, A. Shinbine, T.H. Etsell, P. Sarkar, *J. Ceram. Process. Res.* 12 (2011) 336.

- [34] A.R. Hanifi, A. Torabi, M. Zazulak, T.H. Etsell, L. Yamarte, P. Sarkar, M.C. Tucker, *ECS Trans.* 35 (2011) 409.
- [35] A.R. Hanifi, A. Torabi, X. Chen, S. Hill, P. Sarkar, T.H. Etsell, *J. Electrochem. Soc.* 161 (2014) F391.
- [36] P. Keyvanfar, V. Birss, *ECS Trans.* 57 (2013) 1627.
- [37] A.R. Hanifi, A. Shinbine, T.H. Etsell, P. Sarkar, *Int. J. Appl. Ceram. Technol.* 9 (2012) 1011.
- [38] A. Torabi, A.R. Hanifi, T.H. Etsell, P. Sarkar, *J. Electrochem. Soc.* 159 (2012) B201.
- [39] R.M. Batista, E.N.S. Muccillo, *Ceram. Int.* 37 (2011) 1047.
- [40] R.M. Batista, E.N.S. Muccillo, *Ceram. Int.* 37 (2011) 1929.
- [41] A.L. Vincent, A.R. Hanifi, J.L. Luo, K.T. Chuang, A.R. Sanger, T.H. Etsell, P. Sarkar, *J. Power Sources* 215 (2012) 301.
- [42] T.Z. Sholklapper, V. Radmilovic, C.P. Jacobson, S.J. Visco, L.C. De Jonghe, *Electrochem. Solid-State Lett.* 10 (2007) B74.
- [43] T.Z. Sholklapper, C. Lu, C.P. Jacobson, S.J. Visco, L.C. De Jonghe, *Electrochem. Solid-State Lett.* 9 (2006) A376.
- [44] V.V. Kharton, E.N. Naumovich, A.A. Vecher, *J. Solid State Electrochem.* 3 (1999) 61.
- [45] A. Leonidea, Y. Apela, E. Ivers-Tifféea, in: P. Vanysek, D. Hansen, M. Orazem (Eds.), 215th ECS Meeting, San Francisco, CA, 2009, p. 81.
- [46] P.V. Aravind, J.P. Ouweltjes, J. Schoonman, *J. Electrochem. Soc.* 156 (2009) B1417.